Contributions to Entomology 73 (2) 2023, 269–278 | DOI 10.3897/contrib.entomol.73.e109206

CONTRIBUTIONS TO ENTOMOLOGY

SENCKENBERG

Research Article

Hydraulic engineering of Drusinae larvae: head morphologies and their impact on surrounding flow fields

Ariane Vieira[1], Hendrik C. Kuhlmann[1], Johann Waringer[2], Carina Zittra[2], Simon Vitecek[3,4], Stephan Handschuh[5]

1 *Institute of Fluid Mechanics and Heat Transfer, TU Wien, Getreidemarkt 9/BA, 1060 Vienna, Austria*
2 *Department of Functional and Evolutionary Ecology, University of Vienna, Djerassiplatz 1, 1030 Vienna, Austria*
3 *WasserCluster Lunz, Dr. Kupelwieser-Prom. 5, 3293 Lunz am See, Austria*
4 *University of Natural Resources and Life Sciences, Vienna, Austria*
5 *VetCore Facility for Research, Imaging Unit, University of Veterinary Medicine Vienna, Veterinärplatz 1, 1210 Vienna, Austria*

https://zoobank.org/AA93B5E9-F712-4E72-8DDC-CB5C12BAAADB

Corresponding author: Johann Waringer (johann.waringer@univie.ac.at)

Academic editor: Astrid Schmidt-Kloiber | Received 8 July 2023 | Accepted 22 November 2023 | Published 19 December 2023

Abstract

Body morphologies are significantly different amongst the members of the Drusinae subfamily. Aligned with such differences is the selective niche location chosen by many species from the subfamily. Typically, they live on the sediments of cold, well-oxygenated mountain streams from the Eurasian Region. However, each of the three evolutionary lineages (shredders, grazers and carnivorous filter feeders) inhabit different hydraulic locations according to their foraging behaviour. To investigate the relationship between the body morphology and the flow field near the body, we use Large Eddy Simulations to compute the flow past five different species of the subfamily. We selected species representing the three evolutionary lineages of the subfamily, *Drusus alpinus* Meyer-Dür 1875 from the shredders clade, *D. bosnicus* Klapálek 1899 and *D. monticola* McLachlan 1876 from the grazers clade and *Cryptothrix nebulicola* McLachlan 1867 and *D. discolor* (Rambur 1842) from the filter feeders clade. For the simulations, three-dimensional body shapes were reconstructed from X-ray micro CT data and exposed to a turbulent flow corresponding to water-depth and velocity data measured in the field. The total forces acting on each morphotype were found to be comparable. The lift coefficients computed and ranging from 0.07 to 0.17 are smaller than the drag coefficients which were found to range from 0.32 to 0.55. The local distribution of the skin-friction indicates flow-separation zones near the edges of the bodies, in particular, between the head and the pronotum, which are differently located according to each species. Moreover, we observe higher streamwise normal stresses upstream of the head of the filter feeder species. It is hypothesised that the upstream horseshoe vortex can lift up drifting food particles and transport these to the larvae's filtering legs, thereby enhancing the encounter rates of particles with the filtering devices.

Key Words

ecomorphology, Insecta, larva, numerical flow analysis, Trichoptera

Introduction

We observe a great variety of life forms due to evolution. Through natural selection, different population members are more likely to survive and pass their characteristics to their offspring. As the natural environment is intrinsically transient, previously neutral or harmful characteristic properties may become beneficial, while helpful features may become unfavourable.

* The paper is part of 17th International Symposium on Trichoptera, Edited by Simon Vitecek, Astrid Schmidt-Kloiber, Wolfram Graf, Hans Malicky.

In this context, Drusinae is a highly endemic caddisfly subfamily restricted to Eurasian mountains, where cold running waters provide a well-oxygenated habitat. The subfamily includes three main clades connected to their foraging method: omnivorous shredders, grazers and filtering carnivores (Bohle 1983; Pauls et al. 2008; Graf et al. 2009; Waringer et al. 2010, 2015; Vitecek et al. 2015). Furthermore, Graf et al. (2009) suggest that different clade members inhabit distinct river sections and their distribution follows food availability in the stream bed. This observation is also supported by Waringer et al. (2010) and Waringer et al. (2021). However, no data are available linking the characteristic body shapes of these clades to their environment, even though they have unresolved relationships at the clade level.

In this work, we simulate the flow around different species from the Drusinae subfamily. The goal is to investigate whether changes in body morphology yield significant modifications of the surrounding flow field and, thus, of the forces acting on the body. If such differences exist, they could possibly be favourable for the respective species. To that end, three-dimensional models of larvae are constructed from tomographic data and flow simulations are carried out for two different flow conditions.

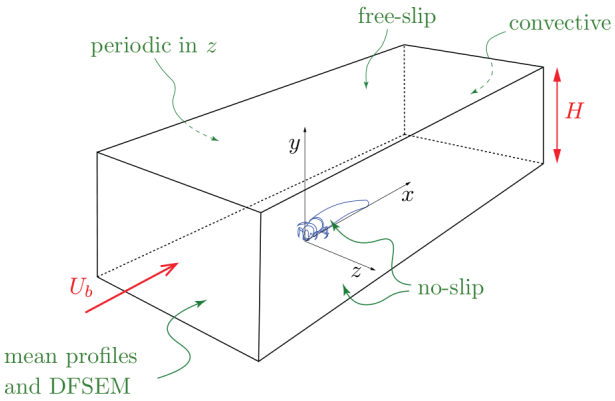

Figure 1. Geometry of the computational domain, coordinate system and boundary conditions.

Methods

Problem formulation

To simulate the flow past different Drusinae species, we use realistic body shapes and resolve the problem numerically in time and space using **OpenFOAM**. To that end, we employed micro-computer tomography (µ-CT) data of different species to construct the body shapes. Based on the larvae's natural setting, a rectangular computational domain in the form of an open channel was created. The reconstructed bodies were then placed in the channel and exposed to a turbulent flow, based on flow velocities measured in situ at the larvae locations. The workflow is illustrated in Fig. 1 where the mean flow is in positive x direction (from left to right). We use a cartesian coordinate system which is aligned with the channel walls. The origin of the coordinate system is placed on the bottom wall exactly beneath the upstream-facing tip of the larva's head (Fig. 1). While the channel height is fixed to H = 25 mm, the elevation of the body varies within 2.20 mm ≤ h ≤ 3.30 mm, depending on the respective larva considered.

The turbulent flow is fully described by the incompressible Navier-Stokes equations and suitable boundary conditions as indicated in Fig. 1. On the surface of the body, as well as on the bottom wall, no-slip boundary conditions are imposed. The top boundary is assumed to be stress-free, emulating a free surface. For computational economy, the channel's side boundaries are considered periodic. The fluid enters the domain in a turbulent state through the inlet with a bulk Reynolds number

$$Re_b = \frac{U_b\, H}{\nu} \qquad (1)$$

where U_b is the bulk (or mean) velocity and ν is the kinematic viscosity ($\nu = 1.31 \times 10^{-6}$ m²/s for water at a temperature of 10.5 °C). At the outlet, we assume zero streamwise gradients of all flow velocities. The numerical solution yields the instantaneous velocity $\vec{u}\,(\vec{x}, t)$ and pressure $p(\vec{x}, t)$ fields. After a transient time, these quantities are averaged to obtain temporal mean values.

Field data

For the flow measurements, nine final instar larvae from Drusinae were selected in their characteristic habitats, representing the three clades of the subfamily (two shredders, four grazers, three filter feeders). The measurements were taken directly in front of the larvae using a tripod mounted Schiltknecht MiniWater 20 Micro velocimeter probe (resolution: 0.01 m/s, probe diameter H_p = 11 mm) with a sampling rate of 1 Hz. The measured velocities ranged from 0 to 0.93 m/s. The total water depths were between 10 mm and 30 mm. Typically, larvae were sitting on top of flattened sediment pebbles, aligned with the flow direction and head upstream. Further information and an analysis of the measured data can be found in Waringer et al. (2021). The present simulations were carried out for the two velocities out of the above range, U_b = 0.55 m/s and U_b = 0.40 m/s.

3D larva models for numerical simulation

We employed micro-computer tomography (µ-CT) to create the external surface of five specimens according to the three different feeding modes prevailing in Drusinae: *Drusus alpinus* Meyer-Dür, 1875 (representing the shredder clade), *D. bosnicus* Klapálek, 1899 and *D. monticola* McLachlan, 1876 (representing the grazer clade) and *D. discolor* (Rambur, 1842) and *C. nebulicola* McLachlan, 1867 (representing the filtering carnivore clade). For µ-CT scans, the merged volume was exported as *.TXM file into **Amira 2019.1** (FEI SAS, Mérignac, France, part of Thermo Fisher Scientific™). Image segmentation was achieved in **Amira 6.5.0** (Visage Imaging, Inc., San Diego, CA, USA). Then we used

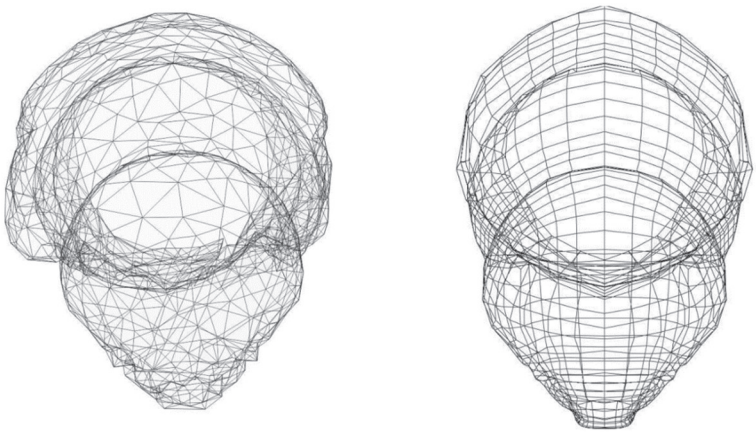

A **B**

Figure 2. A. Original µ-CT data of *Drusus alpinus* (head and pronotum only); **B.** Re-topology of (**A**) used for the flow simulation.

the Amira Surface Generate tool to create the three-dimensional surface renderings. Further information regarding the technical aspects of tomographic scans and a discussion of the three-dimensional tomography reconstruction of the external surface can be found in Zittra et al. (2022).

The surface renderings were further processed using **Blender** to prepare 3D geometries for the numerical simulations. In **Blender**, the original finely triangularised geometry was smoothed and transformed into a symmetric quadrilateral surface mesh. One example of the re-topology is shown in Fig. 2 (head only).

After re-topology of the torso, the legs were moved to a position which resembles the clinging position of the larvae observed in the field. An example is shown in Fig. 3. During the whole processing of the µ-CT data, we tried to preserve the original scale of the animal.

Figure 3. Final position of *Drusus bosnicus* legs.

Numerical simulations

Based on U_b and H from above, the simulation is carried out for bulk Reynolds numbers Re_b = 7634 and Re_b = 10496. Since the flow is expected to be turbulent at these Reynolds numbers, we use Large Eddy Simulation (LES). The turbulent inlet flow is generated by the divergence-free synthetic eddy method (DFSEM) (Poletto et al. 2013). DFSEM needs an auxiliary Reynolds-Averaged-Navier-Stokes simulation (RANS) of the channel flow without the body beforehand. The procedure is illustrated symbolically in Fig. 4 and the set-up follows that of Vieira et al. (2023) for the flow past a wall-mounted cuboid.

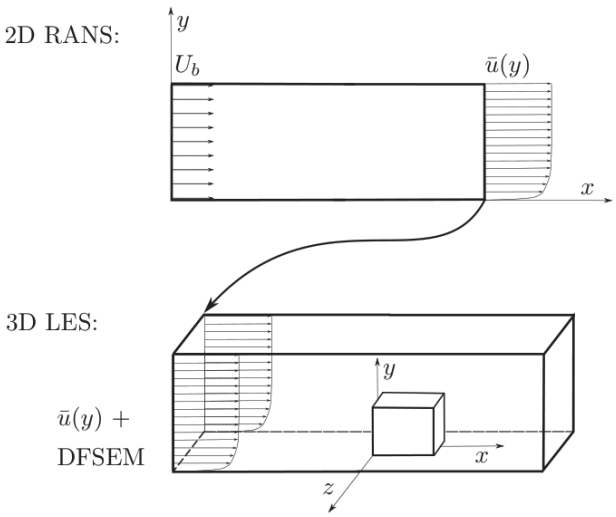

Figure 4. At the top, an auxiliary RANS simulation of a channel flow (without the body). At the bottom, the main LES of the channel flow past the body, symbolically represented by a cuboid.

The simulations are carried out using **OpenFOAM**. This open-source software employs cell-centred finite volumes to discretise the governing equations. The mesh was generated with the tool snappyHexMesh, which requires a cubic hexahedral background mesh (without the body). This background mesh was created with cells of size $\Delta x^+ = \Delta y^+ = \Delta z^+ = \Delta^+_{max} = 11.32$, where the superscript '+' indicates non-dimensional quantities (in wall units). They are based on the friction velocity $u_\tau = \sqrt{\overline{\tau_w}/\rho}$, where $\overline{\tau_w}$ is the mean wall stress of the turbulent flow (here acquired from the auxiliary RANS) and ρ the fluid density. Hence, the non-dimensional velocity, length and time are $\overrightarrow{u^+} = \vec{u}/u_\tau$, $\overrightarrow{x^+} = \vec{x}/(\nu/u_\tau)$, and $t^+ = t\ /\ (H\ /\ u_\tau)$, respectively. The pressure is scaled differently

(see below). In a final step, the mesh was refined locally near the channel floor and the larva's surface reaching $\Delta y^+_{min} = 0.36$. The maximum number of grid points was 6.49×10^6 for *D. monticola* and the minimum was 5.03×10^6 for *C. nebulicola*. A non-dimensional time of $t^+ = 0.44$ was adequate for all field variables to reach a statistically steady state. After that, mean quantities were calculated by averaging over $t^+ \in [0.44,1.75]$.

Results

All flow fields are decomposed into a temporal mean (indicated by an overbar) and a fluctuation (indicated by a prime). For the pressure field $p(\vec{x},t)$, for example, we have

$$p(\vec{x},t) = \bar{p}(\vec{x},t) + p'(\vec{x},t) \qquad (2)$$

where $\bar{p} = (t_1 - t_0)^{-1} \int_{t_0}^{t_1} p(\vec{x},t)dt$ and the mean of the pressure fluctuation $\overline{p'} = 0$ vanishes. For the present calculations, we use $t_0^+ = 0.44$ and $t_1^+ = 1.75$. Characteristic velocities and bulk Reynolds numbers are provided in Table 1.

Table 1. Characteristic velocities and bulk Reynolds numbers.

U_b	Re_b	u_τ	U_L
0.40 m/s	7634	0.022 m/s	0.35 m/s
0.55 m/s	10496	0.030 m/s	0.48 m/s

Flow characteristics upstream the larvae

To analyse the flow past the larva, it is useful to define a local velocity

$$U_L = \frac{1}{1.4\,H\,H_L} \int_0^{H_L} \int_{-0.7H}^{0.7H} \overline{u}(x_0,y,z)dydz, \qquad (3)$$

to which the larva is exposed. The velocity U_L is defined as the mean over the area $[0,H_L] \times [-0.7H,0.7H]$ at the position $x = x_0$ upstream of the larva. Here, we use the height $H_L = 10$ mm $(0.4H)$ which is comparable to the height $H_P = 11$ mm of the velocity probe used to measure the flow velocity in front of the larvae, and $x_0 = -H_L = 0.4H$. Note that the mean elevation of the larvae from the ground is $h = 2.86$ mm which is only a fraction of H_L (Table 2).

Fig. 5 shows the mean velocity profiles $\overline{u}(x_0 = -H_L, y, z = 0)$ in the symmetry plane $z = 0$ upstream of the larva for $Re_b = 10496$. The horizontal dashed line marks the average height $h = 2.86$ mm $(0.286H)$ of the larva models. From Fig. 5 and Table 2, it is seen that the larvae are mainly found in the buffer region $y^+ \in [5,30]$ of the turbulent flow, such that both viscous shear stress and turbulent shear stress are significant to the results.

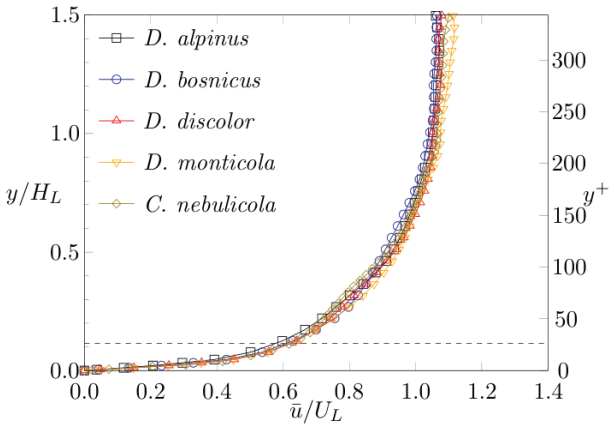

Figure 5. Profiles of the mean velocity $\overline{u}/U_L$ in the mid-plane z as a function of the wall normal distance y/H_L upstream of the larva body at $x_0 = -H_L$. Different species are distinguished by colour and type of symbol. The horizontal dashed line marks the average height of the larva models ($h = 2.86$ mm). Channel with $Re_b = 10496$.

Mean flow fields near the larvae

Fig. 6 shows contours of the streamwise component of the mean velocity $\overline{u}/U_L$ near the larvae for $Re_b = 10496$ and $z = 0$. Generally, the streamwise velocity distribution does not vary much amongst the larvae. In the dark blue regions, the streamwise velocity is negative ($\overline{u} < 0$), indicating the existence of mean recirculation regions. A recirculation region upstream of the larva is a common feature amongst all species and is commonly associated with a horseshoe vortex. Additionally, we recognise a mean recirculation region between the head and the downstream part of the body, which is especially pronounced for *D. bosnicus*. Additional mean recirculation regions are depicted between the posterior area of the body and the bottom wall next to the downstream flow region. In this case, they are more pronounced for *D. bosnicus* and *D. discolor* than for *D. alpinus*.

For a 3D visualisation, we show in Fig. 7 the pressure distribution on the surface of the larvae for $Re_b = 10496$. A common property of all pressure distributions is the high pressure on the forehead of the larvae. In addition, hypersurfaces are shown in cyan on which $\overline{u} = 0$, marking back-flow regions. The extended cyan regions in Fig. 7 suggest a mean recirculating flow exists between the posterior ventral part of the body and the bottom wall for *D. bosnicus*, *D. discolor* and *C. monticola* (Fig. 7B, C,

Table 2. Elevation from the ground h of different larvae in metric units and in wall units (h^+) for each bulk velocity U_b.

Larvae	*D. alpinus*	*D. bosnicus*	*D. discolor*	*D. monticola*	*C. nebulicola*
h	3.30 mm	2.92 mm	2.86 mm	3.05 mm	2.20 mm
h/H_L	0.33	0.292	0.286	0.305	0.22
U_b	h^+	h^+	h^+	h^+	h^+
0.40 m/s	55.6	49.2	48.2	51.4	37.0
0.55 m/s	74.7	66.1	64.8	69.1	49.8

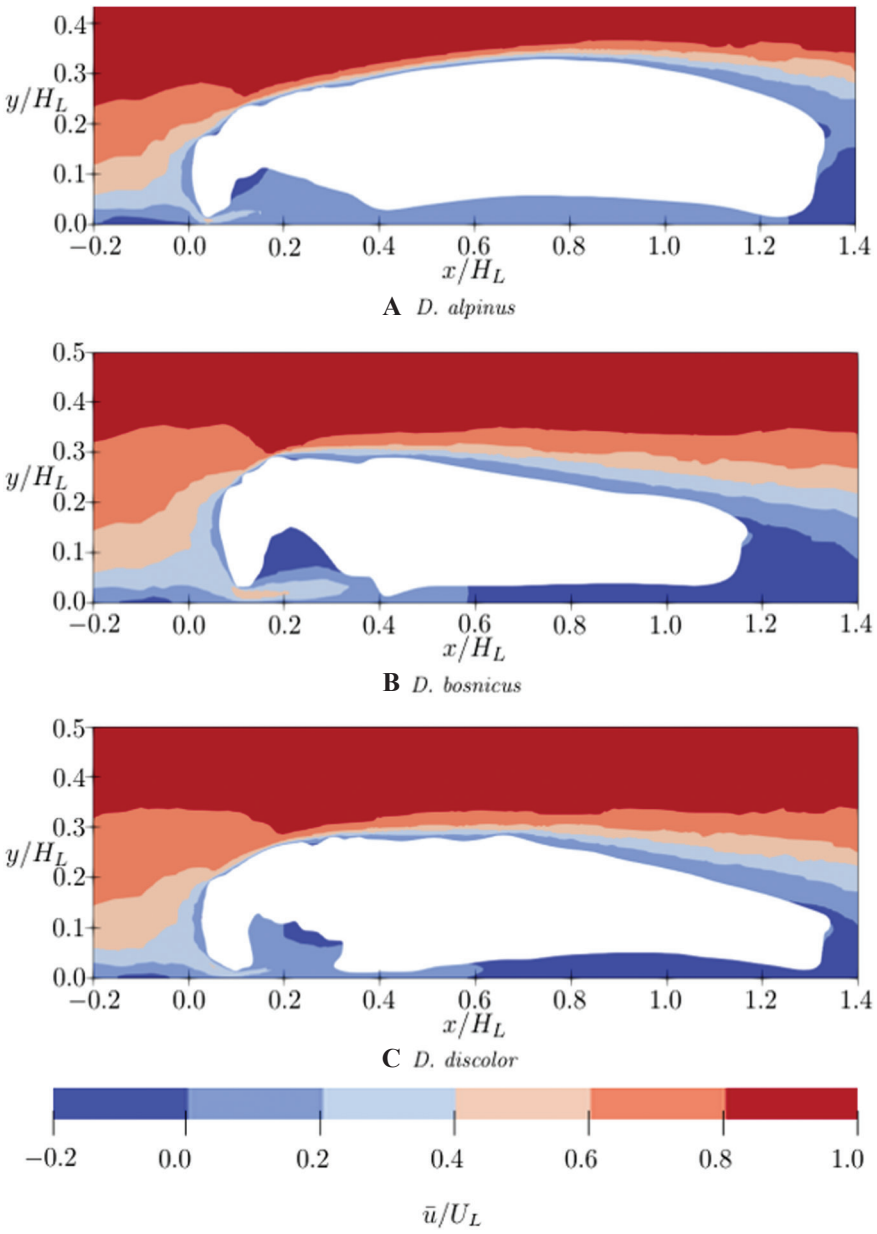

Figure 6. Mean normalised streamwise velocity $\overline{u}/U_L$ in the mid-plane z for Re_b = 10496 and different species as indicated.

D). The reason seems to be related to the body shapes and postures. The back-flow region downstream of the bodies resembles a wake vortex, similar as for other bluff bodies. The wake vortex is not detected for *D. nebulicola* (Fig. 7E), probably because it is significantly smaller than the other species (Table 2) and, thus, is facing a smaller mean velocity over its body height. The body tapering off very gently also tends to suppress a wake vortex. Other smaller recirculation regions arise in body indentations and behind sharp edges, for example, the characteristic pronounced pronotum of *D. bosnicus*.

Drag and lift coefficients

An important question is whether different species perceive different mean forces due to the flow. In the symmetric arrangement considered, only drag $\overline{F_x}$ and lift forces ($\overline{F_y}$) arise. They are usually expressed in terms of the drag and lift coefficients

$$\overline{C_d} = \frac{\overline{F_x}}{(\rho/2)U_L^2 A}, \quad (4)$$

$$\overline{C_l} = \frac{\overline{F_y}}{(\rho/2)U_L^2 A}, \quad (5)$$

which are just the scaled forces. As the scale, we employ the pressure rise $(\rho / 2)U_L^2$ in the forward stagnation point of a body in a homogeneous flow with velocity U_L multiplied by the streamwise projected area of the body (Table 3). Since the forces arise due to the pressure, as

Table 3. Frontal area A from the models, in m^2.

D. alpinus	*D. bosnicus*	*D. discolor*	*D. monticola*	*C. nebulicola*
7.30×10^{-6}	6.15×10^{-6}	5.90×10^{-6}	6.86×10^{-6}	3.59×10^{-6}

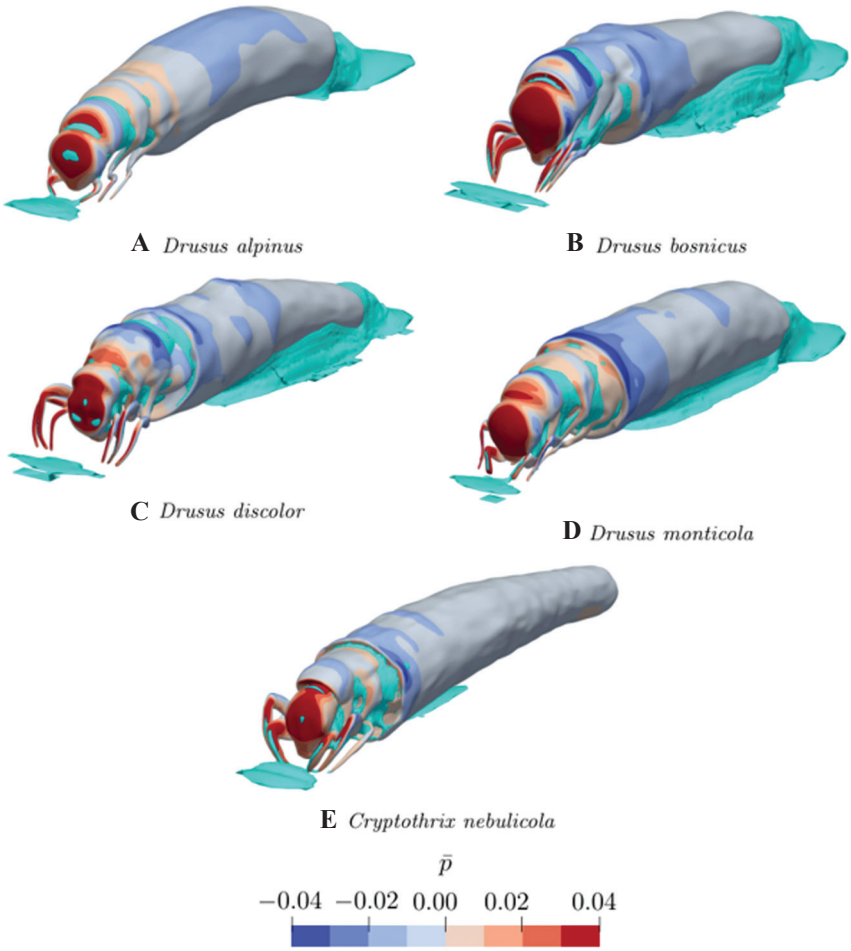

Figure 7. Mean pressure distribution on the surface of the different models for Re_b = 10496 according to the colour bar. Cyan colour indicates three-dimensional hypersurfaces on which the streamwise component of the mean velocity vanishes $\overline{u} = 0$.

well as the viscous stress distributions on the body, we decompose the drag and lift coefficients into a pressure and a viscous part,

$$\overline{C_d} = \overline{C_{d,p}} + \overline{C_{d,v}}, \tag{6}$$

$$\overline{C_l} = \overline{C_{l,p}} + \overline{C_{l,v}}, \tag{7}$$

which are distinguished by the subscripts p (pressure part) and v (viscous part). Note that the viscous normal stress is taken care of by the pressure part.

Fig. 8 shows the mean drag and lift coefficients for all larvae and Reynolds numbers simulated. The pressure and viscous contributions are shown in black and blue, respectively. For Re_b = 7634 the maximum overall drag is found in *C. nebulicola* with a difference of 41% compared to *D. alpinus* (which has the lowest drag value) for the same Reynolds number (Fig. 8A). In the case of Re_b = 10496, the difference between species decreases to ≈ 28% for the drag coefficient, with the lowest value present in *D. alpinus* and the highest in *D. monticola*. The lift coefficients are about 3.5 times smaller than the drag coefficients (Fig. 8B). The highest values are found consistently for *D. bosnicus* for the two Reynolds numbers tested. Additionally, the minimum lift values are found consistently for *C. nebulicola*.

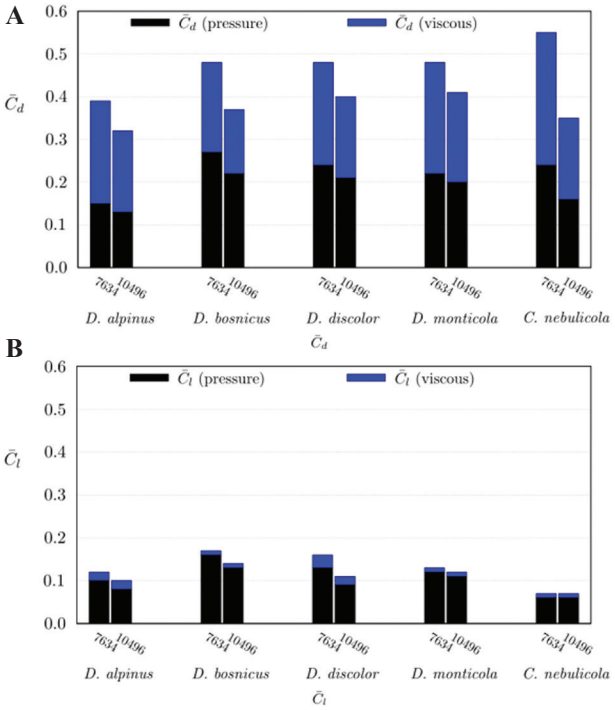

Figure 8. A. Mean drag coefficients $\overline{C_d}$ and **B.** Mean lift coefficients $\overline{C_l}$ as a function of Re_b for individual species (as indicated). Viscous and pressure contributions are indicated by blue and black colour, respectively.

Spatial distribution of normal Reynolds stresses

Fig. 9 shows the Reynolds stress $\overline{u'u'}/u_L^2$, describing the squared magnitude of the fluctuation velocity in the x direction. The Reynolds stress level for *D. discolor* (and for *C. nebulicola*, not shown) is found to be higher than for the other species. In channel flow, the production of turbulent kinetic energy has a maximum near $y^+ = 11$ (Laadhari 2002; Monkewitz 2022). Accordingly, the streamwise velocity fluctuations, measured by $\overline{u'u'}$, also reach their maximum in this region (Lee and Moser 2015). Additionally, the characteristic shape of their bodies, the concave face of *D. discolor* and the high number of edges of *C. nebulicola* might induce flow separation and recirculation, as well as shedding of vortices, which can increase the stresses.

The smallest overall Reynolds stresses $\overline{u'u'}/u_L^2$ are found for *Drusus bosnicus*. A reason could be *Drusus bosnicus* has the smallest length-to-height ratio amongst the species. Furthermore, the tapered shape of the body may create a streamlined silhouette, which may be responsible for stress reduction. Regarding *D. alpinus*, the highest stresses arise past the dorsal line.

Fig. 10 shows the distribution of the streamwise component of the mean skin-friction coefficient $\overline{C_f} = 2\tau_{w,x}/\rho U_b^2$ for $Re_b = 10496$, where $\tau_{w,x} = \overrightarrow{\tau_w} \cdot \overrightarrow{e_x}$ is the x component of the vectorial wall shear stress. We noticed that the mean viscous streamwise surface stress is most pronounced near the edges of the bodies, i.e. at the edge of the head and the pronotum. These are regions from which vortices can be shed into the flow.

Discussion

LES was employed to simulate the flow past five species from Drusinae larvae for two Reynolds numbers representative of their habitats. Body shapes for the numerical

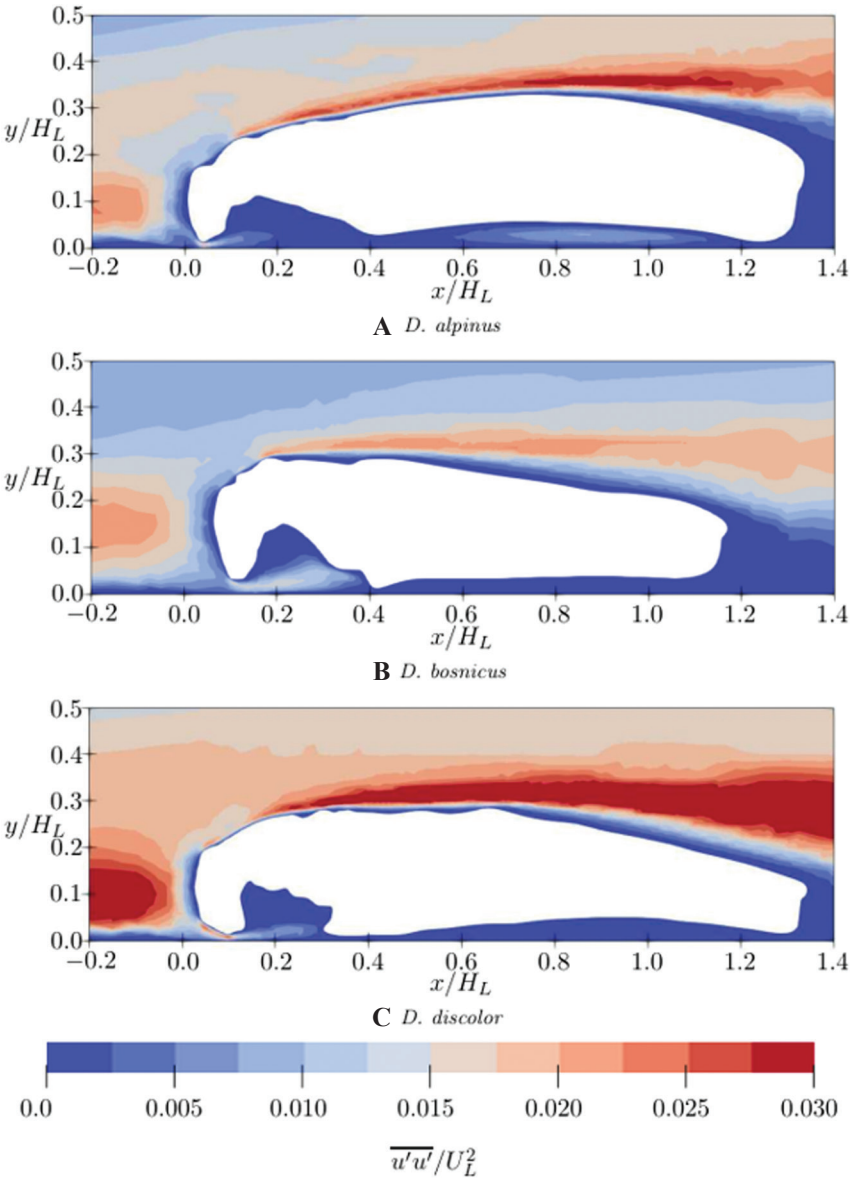

Figure 9. Mean normalised streamwise normal Reynolds stresses $\overline{u'u'}/U_L^2$ in the mid-plane $z = 0$ for $Re_b = 10496$ and different species as indicated.

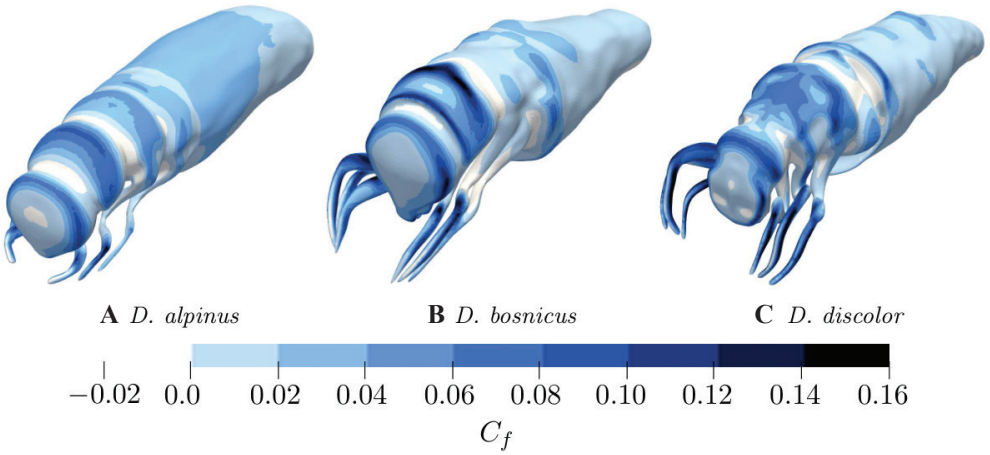

Figure 10. Contours of *x*-component of the skin-friction coefficient for Re_b = 10496 and different morphotypes, as indicated.

simulations were generated from X-ray micro CT data using **Blender**. Mean flow properties, such as drag and lift coefficients and fluctuating properties, such as the streamwise Reynolds stress, were computed and evaluated for flow velocities determined beforehand during field excursions. The larvae are found to be situated in the buffer layer of the turbulent flow where they are subjected to a mean flow as well as to turbulent flow fluctuations. Amongst the fluctuations, the streamwise component is most prominent.

We found that the integral properties, such as the mean drag and the lift coefficients are almost independent of the species. However, local properties like Reynolds stress, skin friction and regions of recirculation vary amongst the species. We speculate the differences are due to the variability in the location of sharp body edges within the species, for example, the characteristically pronounced pronotum of *D. bosnicus*, as well as the shape of their cases. Therefore, body morphology modifications could alter the local flow which could aid their foraging behaviour. For example, the horseshoe vortex created ahead of a larva from the filter-feeders' clade may lift up small food particles drifting on the ground and transport these to the filtering devices (Fig. 11). Future work can deepen the evaluation of these results and integrate them into an ecological context.

Indeed, the results presented here are the first numerical simulations of flow around caddisfly larvae. As such, they are prototypes in this research field and will undergo significant development in the coming years. For instance, we did not incorporate all possible body postures and were not able to account for variation in case shape or material. There is evidence that different body postures are used, for example, for feeding, but body posture and position relative to the direction of flow will also change substantially during larval movement. Moreover, a full-scale analysis of the Drusinae radiation could be conducted, aiming to test whether evolutionary trends can be detected amongst species exposed to similar flow regimes or whether each species has a unique flow niche. Thereby, the evolutionary significance of flow could be explored. To this end, it will be relevant to collect the full flow spectrum to which a Drusinae species' larvae may be exposed through thorough field work.

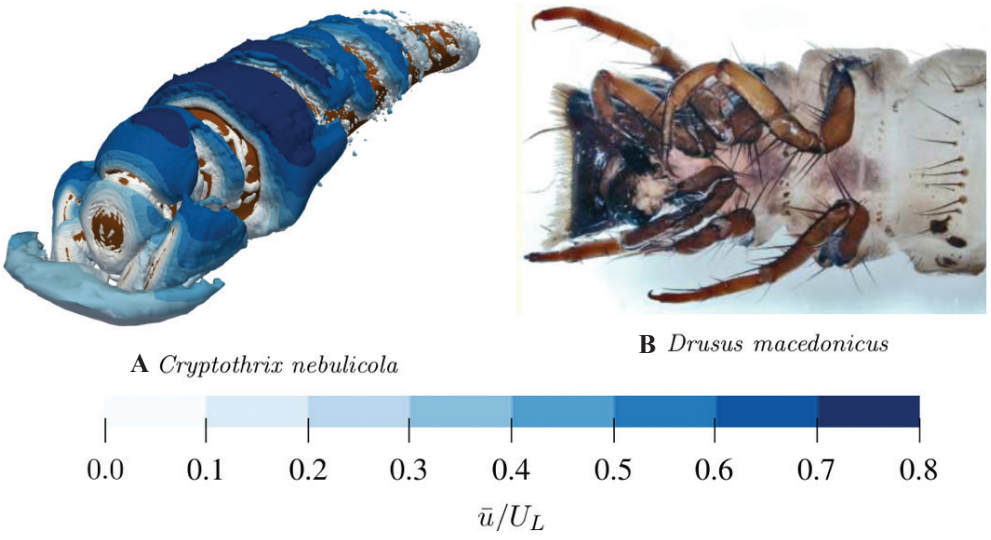

Figure 11. A. Instantaneous vortices detected by the *Q* criterion (second invariant of the mean velocity gradient tensor). The colour code indicates the mean streamwise velocity ($\overline{u}/U_L$); **B.** Filtering devices of *Drusus macedonicus*.

Conflict of interest statement

On behalf of all authors, the corresponding author states that there is no conflict of interest.

Acknowledgements

This paper is part of the project “Intricate bodies in the boundary layer” (project number P31258-B29, PIs: J. Waringer, H. C. Kuhlmann) funded by the Austrian Science Fund (FWF).

References

Bohle H (1983) Driftfang und Nahrungserwerb der Larven von *Drusus discolor* (Trichoptera, Limnephilidae). Archiv für Hydrobiologie 97: 55–470.

Graf W, Waringer J, Pauls S (2009) A new feeding group within larval Drusinae (Trichoptera: Limnephilidae): The *Drusus alpinus* group sensu Schmid, 1956, including larval descriptions of *Drusus franzi* Schmid, 1956, and *Drusus alpinus* (Meyer-Dür, 1875). Zootaxa 2031: 53–62. https://doi.org/10.11646/zootaxa.2031.1.4

Laadhari F (2002) On the evolution of maximum turbulent kinetic energy production in a channel flow. Physics of Fluids 14: L65–L68. https://doi.org/10.1063/1.1511731

Lee M, Moser R (2015) Direct numerical simulation of turbulent channel flow up to $Re_\tau \approx 5200$. Journal of Fluid Mechanics 774: 395–415. https://doi.org/10.1017/jfm.2015.268

Monkewitz PA (2022) Asymptotics of streamwise Reynolds stress in wall turbulence. Journal of Fluid Mechanics 931: A18. https://doi.org/10.1017/jfm.2021.924

Pauls S, Graf W, Haase P, Lumbsch HT, Waringer J (2008) Grazers, shredders and filtering carnivores–the evolution of feeding ecology in Drusinae (Trichoptera: Limnephilidae): insights from a molecular phylogeny. Molecular Phylogenetics and Evolution 46: 776–791. https://doi.org/10.1016/j.ympev.2007.11.003

Poletto R, Revell A, Craft T (2013) A new divergence free synthetic eddy method for LES inflow boundary conditions. Flow, Turbulence and Combustion 91: 519–539. https://doi.org/10.1007/s10494-013-9488-2

Vieira A, Kuhlmann HC, Vitecek S, Handschuh S, Zittra C, Waringer J (2023) Turbulent channel flow past a wall-mounted cuboid (in preparation).

Vitecek S, Graf W, Previšić A, Kučinić M, Olah J, Balint M, Keresztes L, Pauls S, Waringer J (2015) A hairy case: The evolution of filtering carnivorous Drusinae (Limnephilidae, Trichoptera). Molecular Phylogenetics and Evolution 93: 249–260. https://doi.org/10.1016/j.ympev.2015.07.019

Waringer J, Graf W, Pauls S, Previšić A, Kučinić M (2010) A larval key to the Drusinae species (Trichoptera: Limnephilidae) of Austria, Germany, Switzerland and the Dinaric western Balkan. Denisia 29: 383–406.

Waringer J, Graf W, Bálint M, Kučinić M, Pauls S, Previšić A, Keresztes L, Ibrahimi H, Živić I, Stojanović K, Krpač V, Vitecek S (2015) Larval morphology and phylogenetic position of *Drusus balcanicus*, *D. botosaneanui*, *D. serbicus* and *D. tenellus* (Trichoptera: Limnephilidae: Drusinae). European Journal of Entomology 112: 344–361. https://doi.org/10.14411/eje.2015.037

Waringer J, Vitecek S, Martini J, Zittra C, Handschuh S, Vieira A, Kuhlmann HC (2021) Hydraulic niche utilization by larvae of the three Drusinae clades (Insecta: Trichoptera). Biologia 76: 1465–1473. https://doi.org/10.2478/s11756-020-00648-y

Zittra C, Vitecek S, Schwaha T, Handschuh S, Martini J, Vieira A, Kuhlmann HC, Waringer J (2022) Comparing head muscles among Drusinae clades (Insecta: Trichoptera) reveals high congruence despite strong contrasts in head shape. Scientific Reports 12: 1047. https://doi.org/10.1038/s41598-022-04790-2